Anomalous Residual Surface Conductivity in a Superconductor with Strong Spin-Orbit Coupling

J. R. Chamorro[1,2,+], P. Chauhan[2,+], C. Sun[2], N. Varnava[3], M. J. Winiarski[4], N. Ng[1,2], H. K. Vivanco[1,2], L. A. Pressley[1,2], C. M. Pasco[1,2], D. Vanderbilt[3], Yi Li[2], N. P. Armitage[2], and T. M. McQueen[1,2,5,†]

[1]Department of Chemistry, The Johns Hopkins University, Baltimore, MD 21218, USA
[2]Institute for Quantum Matter, Department of Physics and Astronomy, The Johns Hopkins University, Baltimore, MD 21218, USA
[3]Department of Physics & Astronomy, Rutgers University, Piscataway, NJ 08854, USA
[4]Faculty of Applied Physics and Mathematics and Advanced Materials Center, Gdansk University of Technology, ul. Narutowicza 11/12, 80-233 Gdansk, Poland
[5]Department of Materials Science and Engineering, The Johns Hopkins University, Baltimore, MD 21218, USA
[*]mcqueen@jhu.edu
[+]these authors contributed equally to this work

ABSTRACT

Conventional BCS superconductors are expected to exhibit a conductivity with vanishing dissipation as the temperature $T \to 0$ K. While measurements of heat capacity, magnetization, and resistivity indicate $PdPb_2$ is a conventional, type-II superconductor with a T_c of 3.0 K and a bulk gap of $\Delta(0) = 0.370(2)$ meV with $2\Delta(0)/k_BT_c = 2.86$, measurements of surface impedance through microwave cavity perturbation indicate a large, non-vanishing dissipative component below T_c that is at odds with the conventional electrodynamic response of gapped superconductors. By ruling out disorder as an origin of this behavior through extensive sample characterization, we determine $PdPb_2$ to be a candidate topological superconductor with a fully gapped bulk and normal fluid surface, consistent with Majorana surface states. This work highlights the ability of the microwave cavity perturbation technique to detect surface states in topological superconductor candidates.

Introduction

Topological superconductors can host Majorana fermions inside vortex cores and on their surfaces[1]. They have been proposed as platforms for topological quantum computing[2,3]. There are a number of ways of realizing such Majorana fermions, such as topological insulator-superconductor heterostructures[4–8], doping-induced superconductivity in topological insulators[9–12], and superconductivity-proximitized nanowires[13–16]. There are also recent proposals of intrinsic topological superconductors, such as in β-Bi_2Pd[17–19] and $FeTe_{1-x}Se_x$[20–22].

Analogous to a topological insulator, an intrinsic topological superconductor is expected to show surface behavior markedly different from that of the bulk. Topological surface states, if present in the normal state, as is the case in β-Bi_2Pd and $FeTe_{1-x}Se_x$, may be proximitized by the superconducting bulk, and are expected to possess an unconventional, odd-parity gap function that may give rise to Majorana bound states within vortices. Alternatively, under the right symmetry conditions, the bulk of the superconductor may itself be topological, and can give rise to topological surface states below T_c[8]. This kind of topological superconductor is fully gapped in the bulk, but is expected to show non-superconducting surface metallicity. The metallic surfaces in such cases are expected to host Majorana fermions as opposed to massless Dirac fermions, as in topological insulators[8].

Here we present evidence for the existence of non-superconducting metallic surface states in centrosymmetric, tetragonal $PdPb_2$ below its bulk superconducting transition temperature of $T_c = 3$ K. Measurements of the bulk indicate a fully gapped superconducting state, which are in constrast to measurements of the surface impedance through the microwave cavity perturbation technique that indicate significant low frequency dissipation by surface carriers below T_c, an observation contrary to the expectations for a conventional superconductor. Through extensive sample characterization, we rule out extrinsic origins for the observed phenomenology, and propose $PdPb_2$ to be a candidate topological superconductor based on an analysis of the $\mathbb{Z}_2$ invariant of the normal state band structure.

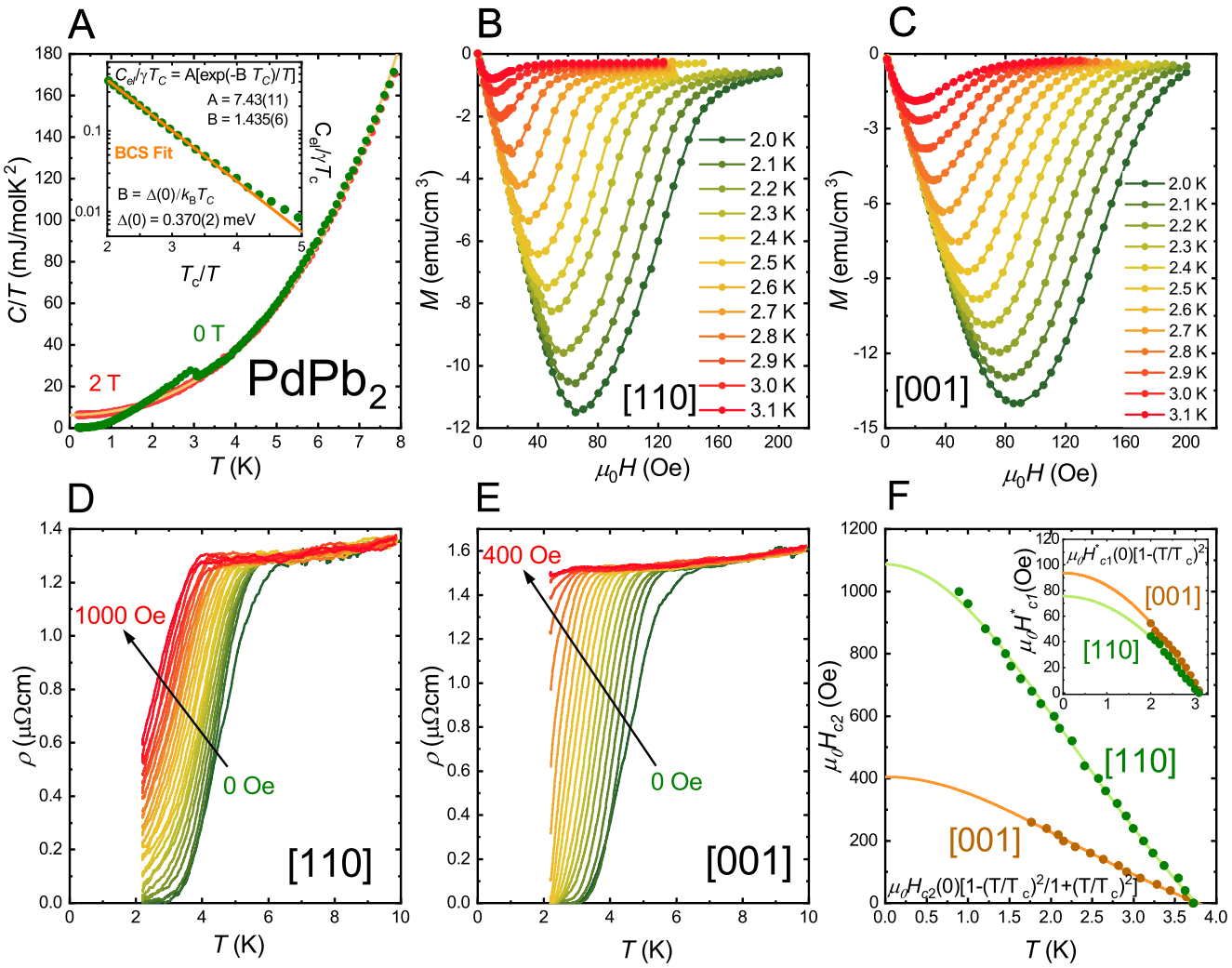

Figure 1. **A** Heat capacity data of $PdPb_2$ at both $\mu_0 H = 0$ T and 2 T. The 2 T data has been fit to determine the electronic and phonon contributions to the heat capacity in the normal state. The inset shows a BCS fit, described in the text, to the $\mu_0 H = 0$ T electronic heat capacity of $PdPb_2$, which indicates a bulk gap of $\Delta(0) = 0.370(2)$ meV. **B** and **C** Field-dependent magnetization curves of $PdPb_2$ at various temperatures, with applied fields along the [110] and [001] directions, respectively. **D** and **E** Temperature-dependent resistivity curves of $PdPb_2$ under various applied fields, with applied fields along the [110] and [001] directions, respectively. **F** Extracted upper critical fields along both directions, using values determined from the fastest slope of the resistivity curves, shown in **D** and **E**. Fits are to the Ginzburg-Landau equation. The inset shows the lower critical fields for both directions, as determined from the magnetization curves after considering demagnetization effects as explained in the Supplementary Material.

Table 1. Superconducting parameters of a $PdPb_2$ crystal oriented along two crystallographic directions relative to the applied field. These include the lower critical field H_{c1}^*, upper critical field H_{c2}, thermodynamic critical field H_c, coherence length $\xi(T=0)$, penetration depth $\lambda(T=0)$, and the Ginzburg-Landau parameter κ. More information is available in the Supplementary Material[25].

Parameter	[110]	[001]
H_{c1}^* (Oe)	75(6)	93(4)
H_{c2} (Oe)	1086(26)	404(17)
H_c (Oe)	191	163
$\xi(T=0)$ (nm)	55	90
$\lambda(T=0)$ (nm)	221	158
κ	4.02	1.75

Results

Bulk Physical Properties

Data from measurements of heat capacity, magnetization, and resistivity of $PdPb_2$ are shown in **Figure 1**. The heat capacity at zero applied magnetic field, shown in **Figure 1 A**, demonstrates a superconducting phase transition at $T_c = 3.0$ K, as per an equal-entropy approximation, in agreement with previous reports[23,24]. An applied field of $\mu_0 H = 2$ T is sufficient to quench this transition down to the lowest measured temperature of $T = 0.2$ K. Fits to the $\mu_0 H = 2$ T data, using $C/T = \gamma + \beta_3 T^2 + \beta_5 T^4$, result in an electronic term $\gamma = 6.32(6)$ mJ/mol K^2, and two phonon terms $\beta_3 = 1.62(1)$ mJ/mol K^4 and $\beta_5 = 0.0184(2)$ mJ/mol K^6. The second phonon term arises from the presence of an Einstein mode with $T_E = 49.5(4)$ K, with fits shown in the Supplementary Material[25]. By subtracting these phonon terms from the $\mu_0 H = 0$ T data, we are able to obtain the electronic heat capacity of $PdPb_2$, C_{el}. After normalizing C_{el} by γ and T_c, we may fit the data to $C_{el}/T = A[\exp(-BT_c)/T]$ in order to obtain the magnitude of the superconducting gap $\Delta(0)$, where A and B are two constants[26], and B is given by $B = \Delta(0)/k_B T_c$ at temperatures $T_c/T \geq 2$. Our fits, shown in the inset of **Figure 1 A** on a log scale, indicate a bulk superconducting gap of $\Delta(0) = 0.370(2)$ meV and a $2\Delta(0)/k_B T_c = 2.86$. The origin of this anomalously small value of $2\Delta(0)/k_B T_c$ in relation to the expected BCS value of 3.53 is unknown. The gap value is in agreement with the value of $\Delta(0) \approx 0.4$ meV obtained via microwave cavity measurements, as discussed below and in the supplementary material[25]. Furthermore, the Sommerfeld coefficient $\gamma \to 0$ as the temperature $T \to 0$ K, marking the absence of a finite residual electronic contribution to the heat capacity in the bulk, as expected for a fully gapped superconductor.

The results of magnetization and resistivity measurements of $PdPb_2$ are shown in **Figure 1 B-F**. Both measurements show a higher onset T_c into a superconducting state compared to heat capacity and microwave perturbation. It is possible that the higher T_c and breadth of the transition are due to superconducting fluctuations above T_c. In order to to rule out extrinsic origins for this behavior, as well as for the surface behavior discussed later in this manuscript, we have performed rigorous measurements of crystal and sample quality, such as powder and single crystal X-ray diffraction, scanning electron microscope imaging, energy-dispersive X-ray spectroscopy, Laue diffraction, and X-ray microtomography, the details of which can be found in the Supplementary Material[25]. Both X-ray diffraction and energy-dispersive X-ray spectroscopy indicate a nominal stoichiometry of $PdPb_2$, with the latter measurement indicating atomic ratios of 33.42(13)% Pd and 66.58(22)% Pb in the best crystal (from which multiple samples were cut and measured).

Measurements were performed on two samples, cut from the same Bridgman-grown crystal, with either the [110] or [001] faces exposed, as determined through Laue diffraction. The extracted superconducting parameters are shown in **Table 1**. The H_{c2} values for both directions, $H_{c2}[110] = 0.1086$ T and $H_{c2}[001] = 0.0404$ T, are much lower than the expected Pauli limit for $PdPb_2$, which through $H_P(\mathrm{T}) \sim 1.85 T_c(\mathrm{K})$, should be approximately $\mu_0 H = 5.5$ T. $PdPb_2$, therefore, does not appear to show signs of triplet pairing or otherwise unconventional superconductivity in the bulk. The derived Ginzburg-Landau parameter $\kappa = \lambda(0)/\xi(0)$, exceeds $\kappa \geq 1/\sqrt{2}$ in both crystallographic directions, indicating $PdPb_2$ is a type-II superconductor.

Microwave Cavity Perturbation Measurements

The microwave cavity perturbation technique was used to determine the temperature-dependent complex surface impedance, $\tilde{Z}_s(T)$, of a single crystal of $PdPb_2$. Measurements were performed in a superconducting NbTi, $T_c \approx 10$ K, cylindrical cavity resonator with a resonance frequency of the TE_{011} mode at 18.66 GHz. The cavity perturbation shifts, marked by a change in complex resonance frequency $\Delta\tilde{\omega}/\omega_0$, were measured upon insertion of the sample. For a sample in the skin depth regime, $\Delta\tilde{\omega}/\omega_0$ can be related to the impedance $\tilde{Z}_s = R_s + iX_s$ via $\frac{\Delta\tilde{\omega}}{\omega_0} = \xi\tilde{Z}_s + \lim_{|\tilde{\sigma}|\to\infty} \frac{\Delta\tilde{\omega}}{\omega_0}$, where ξ is the resonator constant and $\lim_{|\tilde{\sigma}|\to\infty} \frac{\Delta\tilde{\omega}}{\omega_0}$ is the metallic shift[25]. The decomposed surface impedance components, surface resistance R_s and surface reactance X_s, for $PdPb_2$ are shown as a function of temperature in **Figure 2 A**. Both R_s and X_s show a sharp change at $T = 3.0$ K, consistent

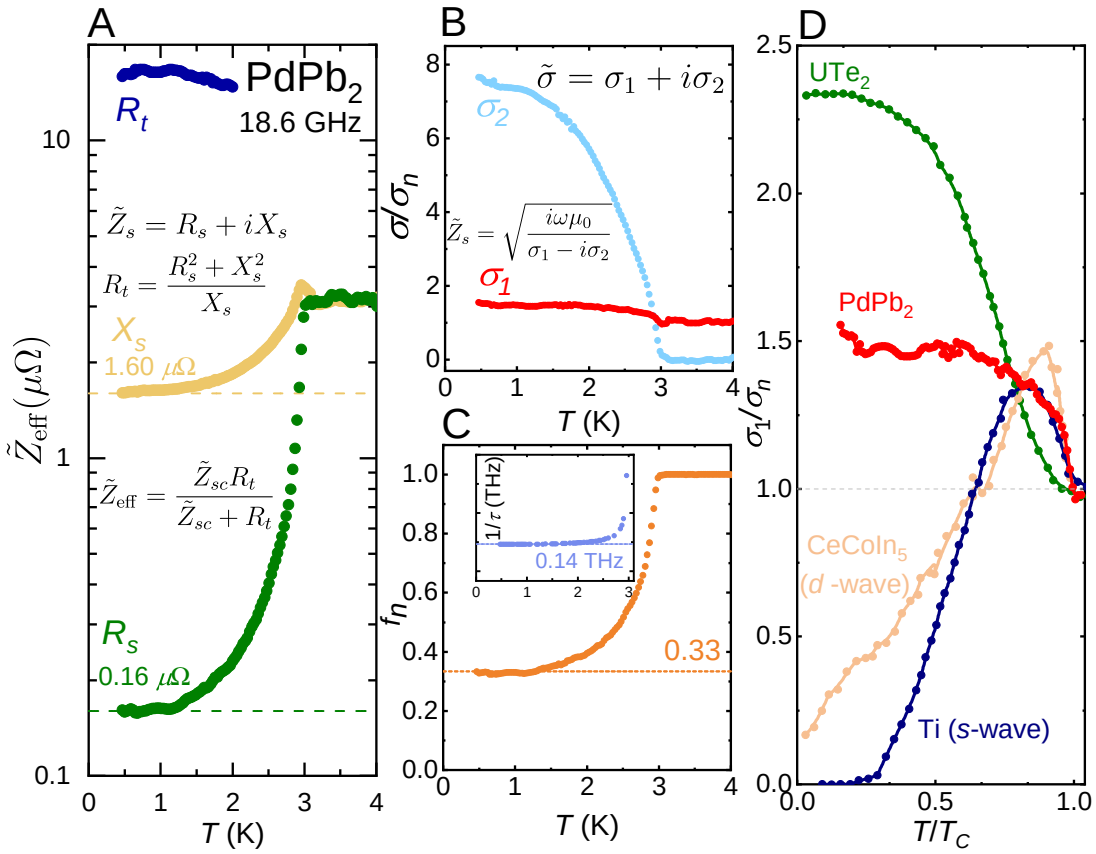

Figure 2. **A** Temperature-dependent complex impedance $\tilde{Z}_{\rm eff}$ of $PdPb_2$. A surface metal sheath with thickness t is considered, giving rise to an effective impedance which arises from both a metal sheath impedance R_t and the impedance of the underlying superconductor Z_{sc}. The real (R_s) normal fluid component of $\tilde{Z}_s$ reaches a finite value of $\sim 0.16\mu\Omega$, contrary to the expectations for a fully gapped superconductor. **B** The effective surface complex conductivity of $PdPb_2$ decomposed as given by $\tilde{\sigma} = \sigma_1 - i\sigma_2$, where σ_1 and σ_2 are the normal fluid and superfluid responses, respectively. σ_1 does not go to zero, as expected for a fully gapped superconductor, and instead increases. **C** The temperature dependence of the fraction of effective normal fluid in $PdPb_2$. This value approaches 33% instead of zero as $T \to 0$ K. The inset shows the extracted value of the scattering rate, which plateaus at 0.14 THz at low temperatures. **D** The real part of the conductivity is shown for several materials, including topological superconductor UTe_2[27], s-wave superconductor Ti[28], d-wave superconductor $CeCoIn_5$[29], and $PdPb_2$. Just as in UTe_2, σ_1 anomalously increases with decreasing temperature. The data for Ti, $CeCoIn_5$, and UTe_2 were extracted from S. Bae, *et.al*.[27]

with a transition into a superconducting state, and reduce with decreasing temperature to plateaued values of $R_s \sim 0.16\ \mu\Omega$ and $X_s \sim 1.60\ \mu\Omega$. The non-zero surface resistance of $\sim 0.16\ \mu\Omega$ implies the presence of a significant dissipative channel that is odds with conventional electrodynamics. As discussed below, it may be consistent with a normal surface fluid when the sample is in superconducting state.

For a bulk homogeneous system, the low temperature dissipation is best quantified via the complex conductivity $\tilde{\sigma}(T)$, which can be extracted in the local electrodynamics regime, from the complex surface impedance by $\tilde{Z}_s = \sqrt{i\omega\mu_0/\tilde{\sigma}}$. The decomposed complex conductivity $\tilde{\sigma} = \sigma_1 - i\sigma_2$, where σ_1 and σ_2 are the normal fluid and superfluid responses, respectively, is shown in **Figure 2 B**. For a conventional superconductor, σ_1 is expected to show a Hebel-Schlicter peak near T_c before decreasing with temperature to a minimum, such that $\sigma_1(0)/\sigma_n = 0$. For d-wave and bulk nodal superconductors, the ratio $0 \leq \sigma_1(0)/\sigma_n \leq 1$ can arise as a result of an underlying nodal gap function. $PdPb_2$, in contrast, shows an anomalous ratio of $\sigma_1(0)/\sigma_n > 1.4$. Even at the lowest measured temperatures of $T_c/T > 3$, the effective value of σ_1 is *greater* than its value in the normal state, indicating that $PdPb_2$ hosts a significant normal dissipative fluid that coexists with fully gapped superconductivity.

The normal fluid components of the effective complex conductivity for several superconductors are shown in **Figure 2 D**, as extracted from S. Bae, *et. al.*[27]. These are effective conductivities, since they are calculated as if the system is homogeneous. In the case of elemental Ti, which is an s-wave superconductor with $T_c = 0.39$ K, σ_1 decreases monotonically to zero as all of $\sigma_n \to \sigma_2$, i.e. all of the normal fluid becomes superfluid below T_c. In the case of $CeCoIn_5$, a known d-wave superconductor, the normal fluid component of the complex conductivity decreases to a finite, non-zero value, as the superconducting gap function possesses nodes. These nodes are sources of dissipation and low energy excitations. Both $PdPb_2$ and topological superconductor candidate UTe_2 show an anomalous response, where σ_1 increases with decreasing temperature and subsequently plateaus. In order to determine whether $PdPb_2$ possesses non-trivial topology in its electronic band structure, we performed density functional theory (DFT) calculations that are discussed below.

The anomalous residual low temperature dissipation could arise either from the bulk or the surface of this material. We investigate each of these possibilities in turn. To further explore the anomalous behavior of the complex conductivity in the case of a homogeneous system, we can describe it using a two-fluid model in terms of the normal fluid and superfluid responses, respectively:

$$\tilde{\sigma}(T) = \frac{ne^2}{m^*}\left(\frac{f_s(T)}{i\omega} + \frac{f_n(T)\tau(T)}{1+i\omega\tau(T)}\right)$$

where n is the total electron density, m^* is the effective mass of the electrons, τ is the effective normal fluid scattering lifetime, f_n is the normal fluid fraction and $f_s = 1 - f_n$ is the superfluid fraction. As τ is always a real positive number, the normal fluid fraction must satisfy $f_n \geq 2/(1+\sqrt{1+(\sigma_2/\sigma_1)^2})$. For conventional superconductors, as $T \to 0$ K, the ratio $\sigma_2/\sigma_1 \to \infty$, implying $f_n \to 0$. As shown in **Figure 2 B**, this ratio approaches $\sigma_2/\sigma_1 \to 5$ in $PdPb_2$ as $T \to 0$, giving a minimum residual normal fluid fraction $f_n \geq 33\%$, i.e. one-third of the normal state value, as shown in **Figure 2 C**. This result is similar to one observed recently in the topological superconductor candidate UTe_2[27]. Again, this is an effective density calculated from a model for the conductivity that assumes that system has a homogeneous electrodynamic response. Similar to UTe_2, $PdPb_2$ possesses significant dissipation on the surface against the backdrop of a fully gapped bulk superconducting state. Furthermore, as shown in the inset of **Figure 2 C**, we determine from the above equation the inverse scattering rate for the anomalous fluid, which decreases to a plateau at low temperature to a value of $\tau^{-1} \approx 0.14$ THz. This value is too low to create an impurity-induced normal fluid scenario.

A possible origin for the anomalous effective conductivity and significant dissipative response is a surface origin of a dissipative normal conduction channel. If the surface of the bulk superconductor has a normal conductor sheath then the expression for extracting a bulk conductivity from the surface impedance becomes invalid. The extracted conductivity can naturally show anomalous features due to contributions from the normal conduction channel. One would need to account for such a thin normal fluid layer at the surface in the effective impedance of the sample. For a thin normal conductor layer with 2D resistance R_t on top of a bulk superconductor with impedance Z_{sc} the effective impedance of the system is given to good approximation by $Z_{\text{eff}} = Z_{sc}R_t/(Z_{sc}+R_t)$[25]. We assume that the bulk superconductor has a purely imaginary impedance $Z_{sc} = iX_{sc}$(reasonable for a fully gapped 3D superconductor at low temperatures). Then normal channel's response follows from the measured signal as $R_t = \frac{R_s^2+X_s^2}{X_s}$. **Figure 2 A** shows the impedance R_t of the thin normal layer with $R_t \sim 16\ \mu\Omega$ for $T \to 0$ K. R_t reduces monotonically with increasing temperature. One can see that it is reasonably temperature independent in the low temperature region where this analysis applies.

Discussion

The DFT calculated electronic band structure, with spin-orbit coupling included, is shown in **Figure 3**. $PdPb_2$ has been predicted to be a symmetry-enforced semimetal with line crossings between the two high symmetry points of the first Brillouin

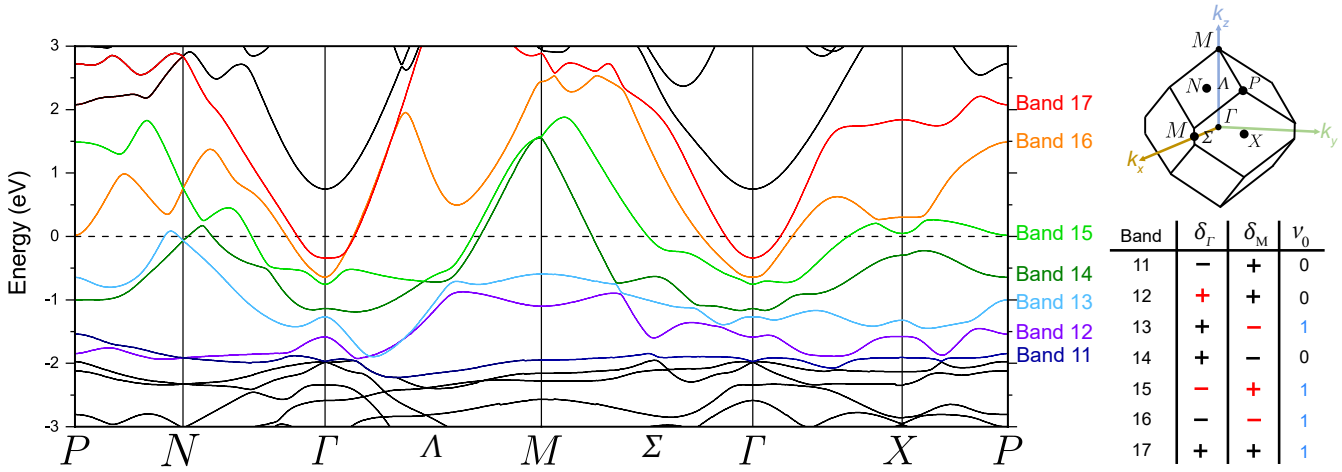

Band	δ_Γ	δ_M	ν_0
11	−	+	0
12	+	+	0
13	+	−	1
14	+	−	0
15	−	+	1
16	−	−	1
17	+	+	1

Figure 3. The calculated electronic band structure of $PdPb_2$, calculated using the local density approximation and with spin-orbit coupling considered. The first Brillouin zone for body-centered tetragonal is shown, under the $a > c$ lattice parameter condition. The parities at $\Gamma(\delta_\Gamma)$ and $M(\delta_M)$ are shown as positive and negative signs. A change in parity from one band to the next is shown in red. The $\mathbb{Z}_2$ topological invariant ν_0 is shown for each band, which is calculated as the product of the parities at Γ and M for that band, along with the product of those two parities for all previous bands. Non-trivial invariants of $\nu_0 = 1$ are shown in blue.

zone Γ and M[30,31]. It has also been predicted to be a topological insulator based on the absence of a linear combination (NLC) of the elementary band representations (EBRs) across the Brillouin zone[30], though it is not an insulator. Our calculated band structure, as well as those previously calculated, indeed show band crossings along the Λ path along k_z between Γ and M, with point group $4mm$. Since $PdPb_2$ possesses time-reversal symmetry, its bulk topology is characterized by a $\mathbb{Z}_2$ invariant[32–34]. As it further possesses inversion symmetry, the $\mathbb{Z}_2$ invariant can be calculated readily by considering the product of the parities of all of the bands up to and including the ones that cross the Fermi level at both Γ and M[35]. Only these two special points in the Brillouin zone determine the topological invariant for body-centered tetragonal, as of the eight time-reversal invariant momentum (TRIM) points in three-dimensions, Γ and M are the only two with odd coefficients $(1\Gamma, 4N, 2X, 1M)$. The band parities at Γ and M, and the resulting topological invariant ν_0, which also considers the product of the parities of all bands beneath the one in question, are shown in **Figure 3**. Our calculations indicate that four of the five bands that cross the Fermi level have non-trivial invariants of $\nu_0 = 1$. $PdPb_2$ is therefore a $\mathbb{Z}_2$ metal in the normal state, a designation also used to describe other topological superconductor candidates such as $FeTe_{1-x}Se_x$[20–22], β-Bi_2Pd[17–19], doped Bi_2Se_3[12,36], Tl_5Te_3[37], and more recently the AV_3Sb_5 (A = K, Rb, and Cs) family of materials[38–41]. More in depth theoretical studies are needed to disentangle the influence of the topological band crossings near the Fermi level on the topology and physical properties.

While our calculations do not reveal the presence of surface states near the Fermi level in the normal state (not shown), the non-trivial invariant of bands that cross the Fermi level in $PdPb_2$ could result in a topological superconductor[42]. Strong spin-orbit coupling arising from the heavy elements Pd and Pb can drive the system into a topological ground state characterized by a fully gapped bulk superconducting state with topologically non-trivial Majorana surface states. We believe that low temperature microwave dissipation is a generic signature of such surface states. $PdPb_2$ therefore adds on to a short list of three-dimensional topological superconductor candidates.

In conclusion, we have discovered an anomalous, large, dissipative surface electrodynamic response in the centrosymmetric superconductor $PdPb_2$. A natural explanation of this phenomenon is that this material is a topological superconductor with surface Majoranas states. The ease with which large, high quality single crystals can be grown can make this material ideal for understanding the origin of this anomalous behavior.

Methods

Crystal Growth

A cylindrical single crystal of $PdPb_2$ of diameter 10 mm and length 50 mm was grown in an evacuated quartz tube via the Bridgman technique. Stoichiometric amounts of Pd (BeanTown Chemical 99.95% trace metals basis) and Pb (Alfa Aesar, 99.999% metals basis) were combined and sealed under vacuum. The sample was heated to approximately 650° C in a GES Corp Ultra-high Temperature Precision Induction Furnace, and moved through the coils at approximately 0.3 mm/hr. The

rotation speed was 10 rpm. Some refinement and purification of the sample was evident post-growth as darker material had collected at the top of the crystal. This was subsequently removed by cutting it off.

Measurement Techniques

Measurements of powder X-ray diffraction were performed on a laboratory Bruker D8 Focus diffractometer (Cu tube, Kα_1: $\lambda = 1.540596$ Å and Kα_2: $\lambda = 1.544493$ Å) with a LynxEye detector. Measurements of single-crystal X-ray diffraction were carried out using a SuperNova diffractometer (Mo Kα radiation, $\lambda = 0.71073$ Å) equipped with an Atlas detector, after mounting a crystal of $PdPb_2$ with a small amount of Paratone-N oil. Rietveld refinements of the powder X-ray diffraction data were performed on TOPAS (Bruker AXS). Refinements of single crystal data were performed using the CrysAlisPro software suite, in conjunction with SHELXS-97[43]. Single crystals were cut using a diamond wire saw and oriented along various crystallographic orientations through the use of a back-reflection Multiwire Laboratories MWL100 Laue diffractometer with a W source.

Measurements of magnetization, heat capacity and electrical resistance were carried out in a Quantum Design Physical Properties Measurement System (PPMS). For magnetization, oriented crystals were measured with the PPMS magnetic field parallel to either the [110] or [001] planes. Four probe resistivity measurements were carried out using silver paste. Measurements of heat capacity below $T = 1.8$ K were enabled by a Quantum Design dilution refrigerator.

Microwave cavity penetration depth experiments were performed in a cylindrical microwave cavity resonator with a resonance frequency of the TE011 mode at 18.6 GHz. An approximately spherical single crystal of $PdPb_2$ was introduced into the magnetic field antinode of the TE011 mode of the cavity. The complex surface impedance of $PdPb_2$ $\tilde{z}_s = R_s + iX_s$, as a function of temperature, was extracted from the change in resonance frequency with and without the sample using the equation $\frac{\Delta\tilde{\omega}}{\omega_0} = \xi\tilde{Z}_s + \lim_{|\tilde{\sigma}|\to\infty}\frac{\Delta\tilde{\omega}}{\omega_0}$, where ξ is the resonator constant and $\lim_{|\tilde{\sigma}|\to\infty}\frac{\Delta\tilde{\omega}}{\omega_0}$ is the metallic shift. More details can be found in the Supplementary Material[25].

Scanning electron microscopic (SEM) images of the surface of a cut and polished crystal of $PdPb_2$ were collected using a JEOL JSM IT100 SEM at 20 keV operating in backscatter mode, and energy-dispersive spectroscopy (EDS) was performed on the same instrument. X-ray micro-computed tomography (μCT) was used to search for large-scale inclusions in arbitrary pieces of $PdPb_2$ cut from the main crystal. These measurements were performed on a Bruker SkyScan 1172 with the source set to 100 kV/100 μA. Frames were collected using a Cu/Al filter and an SHT 11 MP camera, averaging 5 frames per step and 2300 ms of exposure per step. This technique was also used to determine sample dimensions, for resistivity and microwave cavity penetration depth parameters.

Electronic band structure calculations were primarily performed on $PdPb_2$ by means of Density Functional Theory with the local density approximation (LDA), using the Elk all-electron full-potential linearized augmented-plane wave plus local orbitals (FP-LAPW + LO) code[44]. Calculations were also performed using the Vienna Ab Initio Simulation Package (VASP) code. Spin-orbit coupling was included in all calculations.

References

1. Hasan, M. Z. & Kane, C. L. Colloquium: Topological insulators. *Rev. Mod. Phys.* **82**, 3045–3067, DOI: 10.1103/RevModPhys.82.3045 (2010).
2. Lian, B., Sun, X.-Q., Vaezi, A., Qi, X.-L. & Zhang, S.-C. Topological quantum computation based on chiral Majorana fermions. *Proc. Natl. Acad. Sci.* **115**, 10938–10942, DOI: 10.1073/pnas.1810003115 (2018).
3. Ivanov, D. A. Non-Abelian Statistics of Half-Quantum Vortices in *p*-Wave Superconductors. *Phys. Rev. Lett.* **86**, 268–271, DOI: 10.1103/PhysRevLett.86.268 (2001).
4. Xu, J.-P. *et al.* Experimental Detection of a Majorana Mode in the core of a Magnetic Vortex inside a Topological Insulator-Superconductor $Bi_2Te_3/NbSe_2$ Heterostructure. *Phys. Rev. Lett.* **114**, 017001, DOI: 10.1103/PhysRevLett.114.017001 (2015).
5. Sun, H.-H. *et al.* Majorana Zero Mode Detected with Spin Selective Andreev Reflection in the Vortex of a Topological Superconductor. *Phys. Rev. Lett.* **116**, 257003, DOI: 10.1103/PhysRevLett.116.257003 (2016).
6. He, Q. L. *et al.* Chiral Majorana fermion modes in a quantum anomalous Hall insulator–superconductor structure. *Science* **357**, 294–299, DOI: 10.1126/science.aag2792 (2017).
7. Xu, J.-P. *et al.* Artificial Topological Superconductor by the Proximity Effect. *Phys. Rev. Lett.* **112**, 217001, DOI: 10.1103/PhysRevLett.112.217001 (2014).
8. Fu, L. & Kane, C. L. Superconducting Proximity Effect and Majorana Fermions at the Surface of a Topological Insulator. *Phys. Rev. Lett.* **100**, 096407, DOI: 10.1103/PhysRevLett.100.096407 (2008).

9. Wray, L. A. *et al.* Observation of topological order in a superconducting doped topological insulator. *Nat. Phys.* **6**, 855–859, DOI: 10.1038/nphys1762 (2010).

10. Smylie, M. P. *et al.* Evidence of nodes in the order parameter of the superconducting doped topological insulator $Nb_xBi_2Se_3$ via penetration depth measurements. *Phys. Rev. B* **94**, 180510, DOI: 10.1103/PhysRevB.94.180510 (2016).

11. Hosur, P., Ghaemi, P., Mong, R. S. K. & Vishwanath, A. Majorana Modes at the Ends of Superconductor Vortices in Doped Topological Insulators. *Phys. Rev. Lett.* **107**, 097001, DOI: 10.1103/PhysRevLett.107.097001 (2011).

12. Sasaki, S. *et al.* Topological Superconductivity in $Cu_xBi_2Se_3$. *Phys. Rev. Lett.* **107**, 217001, DOI: 10.1103/PhysRevLett.107.217001 (2011).

13. Das, A. *et al.* Zero-bias peaks and splitting in an Al–InAs nanowire topological superconductor as a signature of Majorana fermions. *Nat. Phys.* **8**, 887–895, DOI: 10.1038/nphys2479 (2012).

14. Mourik, V. *et al.* Signatures of Majorana Fermions in Hybrid Superconductor-Semiconductor Nanowire Devices. *Science* **336**, 1003–1007, DOI: 10.1126/science.1222360 (2012).

15. Stanescu, T. D. & Tewari, S. Majorana fermions in semiconductor nanowires: fundamentals, modeling, and experiment. *J. Physics: Condens. Matter* **25**, 233201, DOI: 10.1088/0953-8984/25/23/233201 (2013).

16. Stanescu, T. D., Lutchyn, R. M. & Das Sarma, S. Majorana fermions in semiconductor nanowires. *Phys. Rev. B* **84**, 144522, DOI: 10.1103/PhysRevB.84.144522 (2011).

17. Li, Y., Xu, X., Lee, M.-H., Chu, M.-W. & Chien, C. L. Observation of half-quantum flux in the unconventional superconductor β-Bi2Pd. *Science* **366**, 238–241, DOI: 10.1126/science.aau6539 (2019).

18. Lv, Y.-F. *et al.* Experimental signature of topological superconductivity and Majorana zero modes on β-Bi_2Pd thin films. *Sci. Bull.* **62**, 852–856, DOI: 10.1016/j.scib.2017.05.008 (2017).

19. Sakano, M. *et al.* Topologically protected surface states in a centrosymmetric superconductor β-$PdBi_2$. *Nat. Commun.* **6**, 8595, DOI: 10.1038/ncomms9595 (2015).

20. Zhang, P. *et al.* Observation of topological superconductivity on the surface of an iron-based superconductor. *Science* **360**, 182–186, DOI: 10.1126/science.aan4596 (2018).

21. Xu, G., Lian, B., Tang, P., Qi, X.-L. & Zhang, S.-C. Topological Superconductivity on the Surface of Fe-Based Superconductors. *Phys. Rev. Lett.* **117**, 047001, DOI: 10.1103/PhysRevLett.117.047001 (2016).

22. Machida, T. *et al.* Zero-energy vortex bound state in the superconducting topological surface state of Fe(Se,Te). *Nat. Mater.* **18**, 811–815, DOI: 10.1038/s41563-019-0397-1 (2019).

23. Pattalwar, S. M., Dixit, R. N., Shete, S. Y. & Basu, B. K. Low-temperature specific heat of $PdPb_2$. *Phys. Rev. B* **38**, 7067–7069, DOI: 10.1103/PhysRevB.38.7067 (1988).

24. Havinga, E., Damsma, H. & Hokkeling, P. Compounds and pseudo-binary alloys with the $CuAl_2$(C16)-type structure I. Preparation and X-ray results. *J. Less Common Met.* **27**, 169–186, DOI: 10.1016/0022-5088(72)90028-8 (1972).

25. See supplemental material at [url will be inserted by publisher].

26. Tari, A. *The specific heat of matter at low temperatures* (Imperial College Press, 2003).

27. Bae, S. *et al.* Anomalous normal fluid response in a chiral superconductor UTe_2. *Nat. Commun.* **12**, DOI: 10.1038/s41467-021-22906-6 (2021).

28. Thiemann, M., Dressel, M. & Scheffler, M. Complete electrodynamics of a BCS superconductor with μeV energy scales: Microwave spectroscopy on titanium at mK temperatures. *Phys. Rev. B* **97**, 214516, DOI: 10.1103/PhysRevB.97.214516 (2018).

29. Truncik, C. J. S. *et al.* Nodal quasiparticle dynamics in the heavy fermion superconductor $CeCoIn_5$ revealed by precision microwave spectroscopy. *Nat. Commun.* **4**, 2477, DOI: 10.1038/ncomms3477 (2013).

30. Bradlyn, B. *et al.* Topological quantum chemistry. *Nature* **547**, 298–305, DOI: 10.1038/nature23268 (2017).

31. Vergniory, M. G. *et al.* A complete catalogue of high-quality topological materials. *Nature* **566**, 480–485, DOI: 10.1038/s41586-019-0954-4 (2019).

32. Fu, L., Kane, C. L. & Mele, E. J. Topological Insulators in Three Dimensions. *Phys. Rev. Lett.* **98**, 106803, DOI: 10.1103/PhysRevLett.98.106803 (2007).

33. Moore, J. E. & Balents, L. Topological invariants of time-reversal-invariant band structures. *Phys. Rev. B* **75**, 121306, DOI: 10.1103/PhysRevB.75.121306 (2007).

34. Roy, R. Characterization of three-dimensional topological insulators by two-dimensional invariants. *New J. Phys.* **12**, 065009, DOI: 10.1088/1367-2630/12/6/065009 (2010).

35. Fu, L. & Kane, C. L. Topological insulators with inversion symmetry. *Phys. Rev. B* **76**, 045302, DOI: 10.1103/PhysRevB.76.045302 (2007).

36. Liu, Z. *et al.* Superconductivity with Topological Surface State in $Sr_xBi_2Se_3$. *J. Am. Chem. Soc.* **137**, 10512–10515, DOI: 10.1021/jacs.5b06815 (2015).

37. Arpino, K. E. *et al.* Evidence for Topologically Protected Surface States and a Superconducting Phase in $[Tl_4](Tl_{1-x}Sn_x)Te_3$Using Photoemission, Specific Heat, and Magnetization Measurements, and Density Functional Theory. *Phys. Rev. Lett.* **112**, 017002, DOI: 10.1103/PhysRevLett.112.017002 (2014).

38. Ortiz, B. R. *et al.* New kagome prototype materials: discovery of KV_3Sb_5, RbV_3Sb_5, and CsV_3Sb_5. *Phys. Rev. Mater.* **3**, 094407, DOI: 10.1103/PhysRevMaterials.3.094407 (2019).

39. Ortiz, B. R. *et al.* Superconductivity in the $\mathbb{Z}_2$ kagome metal KV_3Sb_5. *Phys. Rev. Mater.* **5**, 034801, DOI: 10.1103/PhysRevMaterials.5.034801 (2021).

40. Ortiz, B. R. *et al.* CsV_3Sb_5: A $\mathbb{Z}_2$ Topological Kagome Metal with a Superconducting Ground State. *Phys. Rev. Lett.* **125**, 247002, DOI: 10.1103/PhysRevLett.125.247002 (2020).

41. Yang, S.-Y. *et al.* Giant, unconventional anomalous Hall effect in the metallic frustrated magnet candidate, KV_3Sb_5. *Sci. Adv.* **6**, eabb6003, DOI: 10.1126/sciadv.abb6003 (2020).

42. Fu, L. & Berg, E. Odd-parity topological superconductors: Theory and application to $cu_xbi_2se_3$. *Phys. Rev. Lett.* **105**, 097001, DOI: 10.1103/PhysRevLett.105.097001 (2010).

43. Sheldrick, G. M. A short history ofSHELX. *Acta Crystallogr. Sect. A Foundations Crystallogr.* **64**, 112–122, DOI: 10.1107/s0108767307043930 (2007).

44. The elk code is available at http://elk.sourceforge.net/.

Acknowledgements

This work was supported as part of the Institute for Quantum Matter, an Energy Frontier Research Center funded by the U.S. Department of Energy, Office of Science, Office of Basic Energy Sciences, under Award DE-SC0019331. J. R. C. acknowledges support of the Gompf Family Fellowship from the JHU Department of Chemistry. J. R. C. is grateful to M. A. Siegler for assistance collecting single-crystal X-ray diffraction data. This work utilized synthetic capabilities in the Platform for the Accelerated Realization, Analysis, and Discovery of Interface Materials (NSF DMR-1539918), a National Science Foundation Materials Innovation Platform. The Magnetic Properties Measurement System used for data collection was funded by the National Science Foundation, Division of Materials Research, Major Research Instrumentation Program, under Award No. 1828490. The dilution refrigerator was funded by the National Science Foundation, Division of Materials Research, Award No. 0821005. Electronic band structure calculations were conducted using computational resources at the Maryland Advanced Research Computing Center (MARCC).

Author contributions statement

J.R.C. conceived the idea of the experiment. J.R.C., M.J.W., and N.N. grew the crystals, measured physical properties, and performed data analysis. P.C. performed microwave cavity perturbation measurements and interpreted data. H.K.V. and C.M.P. performed SEM and EDS measurements. L.A.P. performed X-ray microtomography measurements. J.R.C., C.S., and N.V. performed electronic band structure calculations. All authors contributed to the writing of the manuscript.